

Inertia-Decoupled Equations for Hardware-in-the-Loop Simulation of an Orbital Robot with External Forces

Hrishik Mishra, Alessandro M. Giordano, Marco De Stefano, Roberto Lampariello and Christian Ott

Abstract—In this paper, we propose three novel Hardware-in-the-loop simulation (HLS) methods for a fully-actuated orbital robot in the presence of external interactions using On-Ground Facility Manipulators (OGFM). In particular, a fixed-base and a vehicle-driven manipulator are considered in the analyses. The key idea is to describe the orbital robot’s dynamics using the Lagrange-Poincaré (\mathcal{LP}) equations, which reveal a block-diagonalized inertia. The resulting advantage is that noisy joint acceleration/torque measurements are avoided in the computation of the spacecraft motion due to manipulator interaction even while considering external forces. The proposed methods are a consequence of two facilitating theorems, which are proved herein. These theorems result in two actuation maps between the simulated orbital robot and the physical OGFM. The chief advantage of the proposed methods is physical consistency without level-set assumptions on the momentum map. We validate this through experiments on both types of OGFM in the presence of external forces. Finally, the effectiveness of our approach is validated through a HLS of a fully-actuated orbital robot while interacting with the environment.

I. INTRODUCTION

Orbital robot, i.e. a manipulator-equipped spacecraft, has emerged as a key mission element in on-orbit servicing and active debris removal [1]–[4]. In orbital robotics, control strategies are broadly classified as underactuated (free-floating) and fully-actuated (free-flying) based on spacecraft actuation [4]. The controller software, which includes navigation, control law, etc. [5], is executed on an On-board Software (OSW) computer for a bespoke orbital robot. Among on-ground validation facilities for OSW, Hardware-in-the-loop Simulation (HLS) approaches have increasingly gained eminence [4] due to their inherent integration of available hardware and software models. In particular, On-ground Facility Manipulators (OGFM) are pivotal for HLS validation [6], [7]. Hence, to meaningfully interface the OSW with HLS facility, it is imperative to generate motion in a physically consistent way.

A classification of the reported HLS facilities is provided in Table. I and is summarized below. In [8], [9], HLS for an underactuated and unforced orbital robot was proposed by exploiting its momentum map conservation and combining a numerical simulation of spacecraft states with a fixed-base OGFM. In an alternative strategy in [9], the orbital manipulator was mounted on a vehicle (another manipulator), which effected the spacecraft motion. In [6], [10], the end-effector poses of fixed-base reference robot and OGFM were modeled with a kinematic constraint and drift-compensation schemes

¹All authors are with Institute of Robotics and Mechatronics, German Aerospace Center (DLR), Weßling, Germany.
 Contact e-mail: hrishik.mishra@dlr.de

TABLE I
 CLASSIFICATION OF HLS FACILITIES FOR ORBITAL ROBOTS

Attribute	Classification
• Dynamic interaction between manipulator and spacecraft	<i>Model-based</i> , F/T sensor
• Spacecraft simulation	<i>Fixed-base (software)</i> , <i>Vehicle-driven</i>
• Vehicle causality	<i>Impedance</i> , <i>Admittance</i>
• Commanded motion	<i>Absolute</i> , <i>Relative</i>

were proposed. The vehicle emulation system II [11] used Force and Torque (F/T) measurements instead of model-based dynamics to command the spacecraft motion, which results from interaction between the orbital manipulator and its spacecraft. A fixed-base HLS approach was used in [12] to simulate a dual-arm orbital robot for contact scenarios. A common attribute of HLS in [8], [12] was the use of a fixed-base OGFM and a vehicle with the satellite-prototype to simulate the relative motion between the test satellite and the orbital robot. In [5, §3], a predefined momentum and kinematic model of a grasped satellite were added to the reduced orbital robot dynamics computation to simulate interaction dynamics. Alternatively, in [7], [13], inertia-coupled Hamel’s equations [14] were integrated using F/T measurements to compute the dynamics of the orbital robot’s spacecraft. In [13], joint positions were commanded to a fixed-base OGFM in admittance causality and the spacecraft motion was numerically simulated. Contrastingly, in [7], the orbital manipulator was considered as an impedance on a vehicle, which effected spacecraft motion in admittance causality. To summarize, in the aforementioned past works, for the free-floating case, reduced dynamics on momentum map level-set were exploited while, the Hamel’s equations were used for the case with external forces. Note that, only the former method is implicitly consistent, i.e. momentum map is conserved.

In this paper, the *emphasized* items from Table I are considered. We use a model-based dynamic interaction between orbital manipulator and spacecraft because the interaction forces depend directly on the HLS state-space, i.e. actual motion in OGFM. Like [9], we also analyse *both* fixed-base and vehicle-driven OGFM, but, for the vehicle, *both* causalities, admittance and impedance, are considered. By describing absolute dynamics, we ensure that the OGFM experiences the correctly computed Coriolis/Centrifugal (CC) forces during HLS validation. An orbital manipulator in impedance causality is considered due to its suitability

for contact-oriented tasks [1]–[3]. To this end, the main result of this paper is obtained by proving equivalence between the Controlled Lagrangians (CL) corresponding to the OGFm and the orbital robot. However, instead of the Hamel’s equations or the reduced dynamics, we exploit the inertia-decoupled structure of the Lagrange-Poincaré (\mathcal{LP}) [15, eq. 2.9] equations to fully describe the orbital robot dynamics and, therefore, include spacecraft-actuation and external forces.

The contributions of this paper are threefold. Firstly, for simulating spacecraft motion, we exploit the block-diagonalized inertia of \mathcal{LP} equations to completely obviate the need for joint acceleration/torque measurements, which can be noisy and bias-prone. In fact, for simulating interaction between manipulator and spacecraft even in presence of external forces, we show that only state-space variables of the HLS are sufficient. Secondly, we extend the physical (momentum) consistency in previous free-floating HLS to the case of a forced orbital robot by using \mathcal{LP} equations to completely describe its dynamics. Finally, we demonstrate the effectiveness of the proposed methods through comparative experiments on *two* OGFm platforms, a fixed-base KUKA Light Weight Robot (LWR-4) and the OOS-SIM [7]. In particular, for the latter case, we also provide experimental results for the HLS of a fully-actuated orbital robot while considering environment interactions.

The layout of the paper is as follows. In Sec. II, the OGFm are introduced. The problem statement of HLS for the orbital robot is described in Sec. III. In Sec. IV, the main idea is proposed using the method of Controlled Lagrangians (CL), and \mathcal{LP} equations are introduced. In Sec. V, we propose two converse theorems for dynamics equivalence and three modalities for simulating spacecraft motion in HLS. In Sec. VI, we provide experimental results, followed by concluding remarks in Sec. VII.

II. ON-GROUND FACILITY MANIPULATORS (OGFM)

A. Fixed-base Manipulator

Def. 1: A fixed-base manipulator is a multibody with n holonomic-joints, see left of Fig. 1. Its configuration is denoted with coordinates, $q \in \mathbb{T}^n$, corresponding to the joint positions and \mathbb{T}^n is a Riemannian manifold with manipulator inertia, $M(q) \in \mathbb{R}^{n \times n}$, as its metric tensor.

Note that, for simplicity, the local isomorphism $\mathbb{T}^n \cong \mathbb{R}^n$, is used in control applications and also, henceforward in this paper. The Lagrangian for this manipulator is $L_1 = \frac{1}{2} \dot{q}^\top M(q) \dot{q} - U(q)$, where $U(q)$ is the gravity potential. The dynamics are written using the Euler-Lagrange operator, $\mathcal{EL}(L_1)$ [15, eq. 2.3] as,

$$\mathcal{EL}(L_1, \dot{q}) := M(q)\ddot{q} + C(q, \dot{q})\dot{q} = \tau_1 + \tau_{1d} + J_1(q)^\top \mathcal{F}_e \quad (1)$$

where $C \in \mathbb{R}^{n \times n}$ is the matrix of joint-space CC terms, and $\tau_1, \tau_{1d} \in \mathbb{R}^n$ are actuation and other lumped torques (including gravity potential torques, i.e. $\frac{\partial U(q)}{\partial q}$), respectively. $J_1(q) \in \mathbb{R}^{6 \times n}$ and $\mathcal{F}_e \in \mathbb{R}^6 \cong \mathfrak{se}(3)^*$ are the manipulator Jacobian and wrench at end-effector, respectively.

B. Vehicle-manipulator

Def. 2: A vehicle-manipulator [16] (Fig. 1, right) is a multibody system consisting of a fixed-base manipulator of n holonomic-joints mounted on a vehicle at a frame $\{\mathcal{B}\}$. The configuration of the manipulator and vehicle are denoted with coordinates, q , and $g_b \in \text{SE}(3)$ (see App.), respectively.

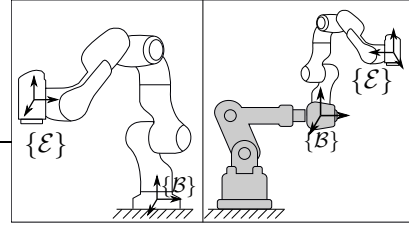


Fig. 1. On-ground facility manipulators. On left, a fixed-base manipulator. On right, a vehicle-manipulator with a mechanical mounting at the industrial manipulator end-effector, $\{\mathcal{B}\}$.

A vehicle might be another manipulator as shown in grey in Fig. 1. For model-based HLS, the vehicle-manipulator can be modeled as a fully-coupled system on the simplified configuration space, $\hat{\mathcal{Q}} \cong \text{SE}(3) \times \mathbb{R}^n$. Considering the gravity potential forces as external, the presence of group coordinate g_b yields a reduced Lagrangian [17, §5] with inertia tensor, $\bar{M}(q) \in \mathbb{R}^{(6+n) \times (6+n)}$, as $\bar{l}_2(q, V) = \frac{1}{2} V^\top \bar{M}(q) V$, where $V = [V_b^\top \quad \dot{q}^\top]^\top$ is the system velocity, $V_b^\wedge \in \mathfrak{se}(3)$ (see App.) is the $\mathfrak{se}(3)$ algebra for the vehicle pose, g_b , and $\dot{g}_b = g_b V_b^\wedge$. Specifically, using \bar{l}_2 , the Hamel’s equations describe the dynamics for the vehicle-manipulator [14, eq. 4.5], which can be obtained using recursive computations [16], and are written in vector algebra notation as,

$$\bar{M}(q) \begin{bmatrix} \dot{V}_b \\ \dot{q} \end{bmatrix} + \bar{C}(V) \begin{bmatrix} V_b \\ \dot{q} \end{bmatrix} = \begin{bmatrix} \bar{\mathcal{F}}_b + \bar{\mathcal{F}}_{bd} \\ \tau_2 + \tau_{2d} \end{bmatrix} + \begin{bmatrix} \bar{J}_b(q)^\top \\ \bar{J}(q)^\top \end{bmatrix} \mathcal{F}_e \quad (2)$$

where, $\bar{\mathcal{F}}_b, \bar{\mathcal{F}}_{bd} \in \mathbb{R}^6 \cong \mathfrak{se}(3)^*$ are the actuation and lumped wrenches (including gravity wrench), of the vehicle, respectively. And, $\tau_2, \tau_{2d} \in \mathbb{R}^n$ are the actuation and lumped torques (including gravity torques) of the manipulator, respectively. Also, $\bar{C} \in \mathbb{R}^{(6+n) \times (6+n)}$ is the non-unique CC dynamic matrix and $\bar{M} = \begin{bmatrix} \bar{M}_b & \bar{M}_{bq} \\ \bar{M}_{bq}^\top & \bar{M}_q \end{bmatrix}$ is the coupled inertia¹. $\bar{J} \in \mathbb{R}^{6 \times n}$, $\bar{J}_b(q) \in \mathbb{R}^{6 \times 6}$ are the end-effector Jacobians for the manipulator and vehicle, respectively, and $\mathcal{F}_e \in \mathbb{R}^6 \cong \mathfrak{se}(3)^*$ is end-effector wrench.

III. THE HLS-PROBLEM FOR AN ORBITAL ROBOT

A. Orbital robot

Def. 3: An orbital robot is a multibody system of $n + 1$ rigid links (including the spacecraft), which are connected with n holonomic-joints. The simplified configuration space of the orbital robot, as seen in Fig. 2 (blue box), is $\hat{\mathcal{Q}} \cong \text{SE}(3) \times \mathbb{R}^n$ with coordinates $z = (g_b, q) \in \hat{\mathcal{Q}}$.

As in Sec. II-B, we also obtain a reduced Lagrangian for the orbital robot with the same system velocity

¹ $\bar{M}_b, \bar{M}_{bq}, \bar{M}_q$ are the locked, coupling and manipulator inertias, respectively [7].

V , but with an inertia tensor, $\hat{M}(q) \in \mathbb{R}^{(6+n) \times (6+n)}$, as $\hat{l}_2(q, V) = \frac{1}{2} V^\top \hat{M}(q) V$. The Hamel's equations describe its dynamics as,

$$\begin{bmatrix} \hat{M}_b & \hat{M}_{bq} \\ \hat{M}_{bq}^\top & \hat{M}_q \end{bmatrix} \dot{V} + \hat{C}(q, V) V = \begin{bmatrix} \hat{\mathcal{F}}_b \\ \hat{\tau} \end{bmatrix} + \begin{bmatrix} \hat{J}_b(q)^\top \\ \hat{J}(q)^\top \end{bmatrix} \mathcal{F}_e, \quad (3)$$

such that (3) has the same form as (2), however, without lumped torques/wrenches, and the corresponding terms are denoted with $(\hat{\bullet})$ instead of (\bullet) .

Remark 1: The fixed-base OGFm in Def. 1 is capable of executing only the motion of an orbital robot's manipulator. So, the spacecraft pose, g_b , is entirely reconstructed in software using the simulated actuation $\hat{\mathcal{F}}_b$, and we denote this HLS configuration space as $\mathcal{Q} = \text{SE}(3) \times \mathbb{R}^n$.

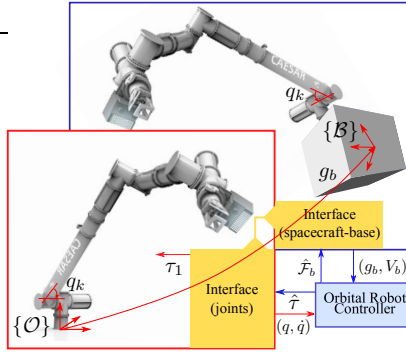


Fig. 2. Diagram of an orbital robot (CAESAR [18], blue) on right. The forced dynamics of this system can be simulated on a fixed-base CAESAR manipulator (red) for HLS validation.

B. Problem Statement

Orbital robots can have a total arm length of 2 – 4[m] [1], [18] depending on mission requirements. Firstly, the HLS validation of these unwieldy-sized robots while using a vehicle-manipulator poses additional complexities [4], which can be avoided using a fixed-base setup. This is illustrated in Fig. 2, where an OBSW is interfaced with the fixed-base CAESAR arm [18] (red box). Secondly, for HLS validation of sensor-based navigation, physical floating-base dynamics is also necessary. In this case, a scaled-down model might be used in a vehicle-manipulator. Therefore, in both cases outlined above, a common interface (Fig. 2, yellow) between an OBSW and OGFm is required, which maps the controller torques, $(\hat{\mathcal{F}}_b, \hat{\tau})$, to that of OGFm, such that the latter's state-space trajectories are identical to that of the orbital robot.

Past HLS methods have relied on Hamel's equations for simulating the forced dynamics of the orbital robot. On one hand, this requires \ddot{q} or τ measurements for reconstructing spacecraft motion (first row in (3)), which is a sensory overhead for the HLS. On the other hand, the Hamel's equations lack the momentum consistency of free-floating dynamics. Note that free-floating dynamics are physically consistent due to the momentum map level-set constraint but are restricted to an unforced case. Therefore, an alternative complete description of the orbital robot is required, which preserves consistency.

IV. MAIN IDEA

A. Method of Controlled Lagrangians

In this paper, we use the method of Controlled Lagrangians (CL) [15], [19]. Its basic idea is as follows: Given the problem to asymptotically stabilize an equilibrium of a mechanical system, we find a control law such that the closed-loop dynamics emerge from a chosen Lagrangian. The method of CL leads to an actuation mapping, which is the key concept used in this paper. For control synthesis details, we refer the reader to [19, §2.2.1].

Firstly, we specify that in contrast to control synthesis, it has to be *proved* that the CLs for the HLS OGFm and the orbital robot are equivalent for the chosen actuation mapping. This is exactly analogous to stating the converse theorem for CL-equivalence [15, Prop. 2.4]. Secondly, the coordinates (z) of the orbital robot in Sec. III are *assumed* identical to those used in and Sec. II-A and Sec. II-B. However, the configuration spaces are different (see Fig.3), i.e. $\hat{\mathcal{Q}} \neq \mathcal{Q}, \bar{\mathcal{Q}}$, because the inertia tensors, which depend on kinematic/dynamic parameters, are different. An OBSW designed for (3) can be meaningfully interfaced with OGFm, if and only if, the time-trajectories of z (red dot) in OGFm (dashed blue) and orbital robot (dashed pink) are identical. This is effected by creating a configuration-dependent mapping between the actuation in cotangent spaces of $\hat{\mathcal{Q}}$ (pink) and $\mathcal{Q}, \bar{\mathcal{Q}}$ (blue), and is the main idea of this paper.

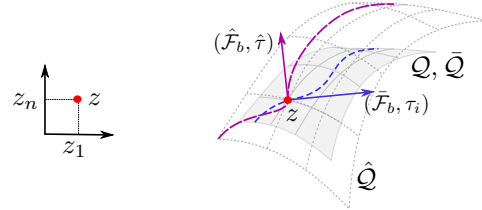


Fig. 3. At any given time, the configuration (red dot) of the mechanical systems in $\hat{\mathcal{Q}}$ (dotted) and $\mathcal{Q}, \bar{\mathcal{Q}}$ (grey) have the same local coordinates z and identical time-trajectories. To achieve this, a mapping between $(\hat{\mathcal{F}}_b, \hat{\tau}_i)$, $i = [1, 2]$ (blue) and $(\hat{\mathcal{F}}_b, \hat{\tau})$ (pink) has to be enforced.

Although this idea can also be applied to the Hamel's equations, (2) and (3), the coupled inertia leads to the problem described in Sec. III-B. So, alternatively, we use \mathcal{LP} equations, which reveal a block-diagonal inertia.

B. Lagrange-Poincaré equations for decoupling Inertias

In this section, the corresponding \mathcal{LP} equations for the vehicle-manipulator and the orbital robot are derived. These equations reveal a block-diagonalized inertia, and hence can be written as a pair of Euler-Poincaré (\mathcal{EP}) and Euler-Lagrange (\mathcal{EL}) equations, which correspond to locked and shape dynamics, respectively [17, §5.3]. First, we demonstrate the concept for the orbital robot and the steps are repeated for the vehicle-manipulator. The \mathcal{LP} equations [17, §5.3] describe the dynamics using a new system velocity $\xi = [\mu^\top \quad \dot{q}^\top]^\top \in \mathbb{R}^{6+n}$ with locked velocity, μ , which is obtained as $\mu = V_b + \hat{A}_l(q)\dot{q}$, where $\hat{A}_l = \hat{M}_b^{-1} \hat{M}_{bq}$.

The locked velocity, μ , has a physical interpretation of being the velocity of the instantaneous equivalent rigid body

system by locking the joints of the orbital robot, and \mathcal{A}_l is known as the local *mechanical connection* in differential geometry [17, §5.3] and the *dynamic-coupling* factor [20] in orbital robotics. The commonly-known generalized momentum, \mathcal{J} , is related to μ as $\mathcal{J} = \text{Ad}_{g_b}^{-\top} \hat{M}_b \mu$.

A key consequence of defining the new system velocity, ξ , is a block-diagonal inertia [21], which leads to a decoupled reduced Lagrangian, $\hat{l}(q, \xi)$. The dynamics resulting from \hat{l} are the \mathcal{LP} equations [17, §5.3], and are obtained as follows. Firstly, note that a linear transformation of V leads to ξ , as $\xi = \hat{T}(q)V$, where $\hat{T} = \begin{bmatrix} \mathbb{I}_{6,6} & \hat{\mathcal{A}}_l \\ 0_{n,6} & \mathbb{I}_{n,n} \end{bmatrix}$. Secondly, using \hat{T} , a dynamic transformation of (3) is obtained, see [21, eq. 15-18], to get the \mathcal{LP} equations as,

$$\begin{bmatrix} \hat{M}_b(q) & 0_{6,n} \\ 0_{n,6} & \hat{\Lambda}_q(q) \end{bmatrix} \begin{bmatrix} \dot{\mu} \\ \dot{q} \end{bmatrix} + \begin{bmatrix} \hat{\Gamma}_b(V) & \hat{\Gamma}_{bq}(V) \\ -\hat{\Gamma}_{bq}(V)^\top & \hat{\Gamma}_{qq}(V) \end{bmatrix} \begin{bmatrix} \mu \\ \dot{q} \end{bmatrix} = \begin{bmatrix} \hat{\mathcal{F}}_b + \hat{J}_b^\top \mathcal{F}_e \\ \hat{\tau} - \hat{\mathcal{A}}_l^\top \hat{\mathcal{F}}_b + \hat{J}_g^\top \mathcal{F}_e \end{bmatrix} \quad (4)$$

where $\hat{J}_g = \hat{J} - \hat{J}_b \hat{\mathcal{A}}_l$ is the end-effector generalized Jacobian, $\hat{\Gamma}_{(\bullet)}$ are the transformed CC terms, and $\hat{\Lambda}_q$ is the reduced inertia matrix [20]. The top and bottom of (4) are the momentum and reduced joint dynamics [20], respectively.

Lemma 1: The top row of \mathcal{LP} equations, (4), are written in a simpler Euler-Poincaré form as,

$$\mathcal{EP}(l, \xi) := \frac{d}{dt}(\hat{M}_b \mu) - \text{ad}_{(\mu - \hat{\mathcal{A}}_l \dot{q})}^\top \hat{M}_b \mu = \hat{\mathcal{F}}_b + \hat{J}_b^\top \mathcal{F}_e \quad (5)$$

where $\mathcal{EP}(l)$ is related to the locked kinetic energy, $l = \frac{1}{2} \mu^\top \hat{M}_b(q) \mu$ and ad_{\bullet} operator is defined in Appendix.

Proof: The unforced momentum equation is [22, eq. 6],

$$\left\langle \frac{dp}{dt}, \eta \right\rangle = \langle p, [(-\hat{\mathcal{A}}_l \dot{q} + M_b^{-1} p)^\wedge, \eta^\wedge]^\vee \rangle, \quad \eta \in \mathbb{R}^6 \quad (6)$$

where $p = \hat{M}_b \mu$ is the momentum referenced at $\{\mathcal{B}\}$. Moving η to the left on L.H.S and R.H.S after using SE(3) bracket isomorphism, $[X^\wedge, \bullet]^\vee = \text{ad}_X$, $X \in \mathbb{R}^6$ (see App.), substituting p and eliminating η yields the L.H.S in (5). To this, the wrench in R.H.S of top row in (4) is added to get (5). ■

Also, the second row in (4) can be compactly written as,

$$\mathcal{EL}(L, \xi) := \hat{\Lambda}_q \ddot{q} + \hat{\Gamma}_q(V) \xi = \hat{\tau} - \hat{\mathcal{A}}_l^\top \hat{\mathcal{F}}_b + \hat{J}_g^\top \mathcal{F}_e \quad (7)$$

where $\hat{\Gamma}_q(V) = \begin{bmatrix} -\hat{\Gamma}_{bq}^\top & \hat{\Gamma}_{qq} \end{bmatrix}$, and $\mathcal{EL}(L)$ corresponds to the shape part of \hat{l} , i.e. $L = \frac{1}{2} \dot{q}^\top \hat{\Lambda}_q(q) \dot{q}$. The spacecraft pose g_b is reconstructed as,

$$\dot{g}_b = g_b (\mu - \hat{\mathcal{A}}_l(q) \dot{q})^\wedge \quad (8)$$

Next, we follow the above steps to rewrite the dynamics of the vehicle-manipulator. We define the *mechanical connection*, $\bar{\mathcal{A}}_l = \bar{M}_b^{-1} \bar{M}_{bq}$ to obtain a linear transformation $\bar{T}(q) = \begin{bmatrix} \mathbb{I}_{6,6} & \bar{\mathcal{A}}_l(q) \\ 0_{n,6} & \mathbb{I}_{n,n} \end{bmatrix}$, and get $\bar{\xi} = [\bar{\mu}^\top \quad \dot{q}^\top]^\top = \bar{T}(q)V$, where $\bar{\mu}$ is the locked velocity. Applying this transformation on (2), we get the momentum equation like in (5) as,

$$\mathcal{EP}(l_2, \bar{\xi}) := \frac{d}{dt}(\bar{M}_b \bar{\mu}) - \text{ad}_{(\bar{\mu} - \bar{\mathcal{A}}_l \dot{q})}^\top \bar{M}_b \bar{\mu} = \bar{F}_b + \bar{J}_b^\top \mathcal{F}_e \quad (9)$$

where $\bar{F}_b = \bar{F}_b + \bar{F}_{bd}$, and $\mathcal{EP}(l_2, \bar{\xi})$ corresponds to the locked kinetic energy, $l_2 = \frac{1}{2} \bar{\mu}^\top \bar{M}_b(q) \bar{\mu}$. Also, this transformation leads to a decoupled shape-space dynamics of the vehicle-manipulator, which is compactly written as,

$$\mathcal{EL}(L_2, \bar{\xi}) := \bar{\Lambda}_q \ddot{q} + \bar{\Gamma}_q \bar{\xi} + \bar{\mathcal{A}}_l^\top \bar{F}_b = \tau_2 + \tau_{2d} + J_2^\top \mathcal{F}_e \quad (10)$$

where $\bar{\Lambda}_q, \bar{\Gamma}_q$ assume the same definitions as in (7) and $J_2(q) = \bar{J} - \bar{J}_b \bar{\mathcal{A}}_l$ is the end-effector generalized Jacobian.

By following the above procedure, the two pairs, (5),(7) and (9),(10) have decoupled inertias. This removes acceleration dependencies between the two equations in each pair, and this addresses the problem described in Sec. III-B.

V. PROPOSED METHOD AND MODALITIES

A. Dynamics equivalence

The main objective of this section is to establish conditions of equivalence between dynamics of an orbital robot and OGF. To this end, we first state the following.

Assumption 1: For the systems in Sections II-III, the initial state-space, $(q(0), \dot{q}(0), g_b(0), \mu(0))$, are identical.

The following two theorems result in the actuation maps that are required for dynamics equivalence.

Theorem 1: (Converse matching for \mathcal{EL} equations): Given shape (joints) dynamics of an orbital robot in (7) and fixed-base OGF ($i = 1$) in (1) and vehicle-manipulator OGF ($i = 2$) in (10), respectively, they produce the same equations of motion, i.e. $(q(t), \dot{q}(t))$, if and only if, Ass. 1 holds and,

- There is a map between the control torques $\tau_i, \hat{\tau}$ as,

$$\begin{aligned} \tau_i = & \mathcal{EL}(L_i, X) - \tau_{id} - \partial_{\dot{q}\dot{q}}(L_i) \hat{\Lambda}_q^{-1} \mathcal{EL}(L, \xi) \\ & + \partial_{\dot{q}\dot{q}}(L_i) \hat{\Lambda}_q^{-1} (\hat{\tau} - \hat{\mathcal{A}}_l(q)^\top \hat{\mathcal{F}}_b) \\ & + (\partial_{\dot{q}\dot{q}}(L_i) \hat{\Lambda}_q^{-1} \hat{J}_g^\top - J_i^\top) \mathcal{F}_e \end{aligned} \quad (11)$$

where $\partial_{\dot{q}\dot{q}}(L_i) = \frac{\partial^2 L_i}{\partial \dot{q}^2}$, $i = 1, 2$ corresponding to (1) and (10), respectively. For $i = 1$, $X = \dot{q}$ and for $i = 2$, $X = \bar{\xi}$.

Proof: Like [19, Prop. 2.1.5], we denote the resulting accelerations in CLs, L_i and L , as $\ddot{q}_i, \ddot{q}_\alpha$ corresponding to actuation torques $\tau_i, \hat{\tau}$, respectively. Taking the inertia-scaled difference in these accelerations, we obtain,

$$\begin{aligned} \hat{\Lambda}_q (\ddot{q}_\alpha - \ddot{q}_i) = & -\mathcal{EL}(L, \xi) + \hat{\tau} - \hat{\mathcal{A}}_l^\top \hat{\mathcal{F}}_b + \hat{J}_g^\top \mathcal{F}_e \\ & - \hat{\Lambda}_q \partial_{\dot{q}\dot{q}}(L_i)^{-1} (-\mathcal{EL}(L_i, X) + \tau_i + \tau_{id} + J_i^\top \mathcal{F}_e) \end{aligned} \quad (12)$$

If τ_i is chosen as (11) and substituted in (12), we get, $\hat{\Lambda}_q(q) (\ddot{q}_\alpha - \ddot{q}_i) = 0_n$. In addition to this equality, if and only if, Ass. 1 holds true, we get identical trajectories for $(q(t), \dot{q}(t))$, thereby proving equivalence of L_i, L . ■

To illustrate the result, for example, applying Theorem 1 on a fixed-base OGF ($i = 1$) in (1), we get,

$$\begin{aligned} \tau_1 = & C(\dot{q}) \dot{q} - \tau_d - M \hat{\Lambda}_q^{-1} \Gamma_q(V) \xi + \\ & M \hat{\Lambda}_q^{-1} (\hat{\tau} - \hat{\mathcal{A}}_l^\top \hat{\mathcal{F}}_b) + (M \hat{\Lambda}_q^{-1} \hat{J}_g^\top - J_i^\top) \mathcal{F}_e \end{aligned} \quad (13)$$

This means that Theorem 1 enforces an interface between the OBSW and the OGF such that the joint-space trajectories of *both* robots in Fig. 2 are identical. Theorem 1 also guarantees that the state-feedback (q, \dot{q}) (red arrow) to the OBSW is consistent with expected orbital robot dynamics.

Theorem 2: (Converse matching for \mathcal{EP} equations): Given locked dynamics of an orbital robot in (5) and vehicle-manipulator in (9), they produce the same equations of motion, i.e. $(g_b(t), \mu(t))$, if and only if, Ass. 1 holds and,

- There is a map between the control torques $\hat{\mathcal{F}}_b, \hat{\mathcal{F}}_b$ as,
$$\begin{aligned} \bar{\mathcal{F}}_b = & -\bar{\mathcal{F}}_{bd} + \mathcal{EP}(l_2, \xi) - \bar{M}_b \hat{M}_b^{-1} \mathcal{EP}(l, \xi) \\ & + \bar{M}_b \hat{M}_b^{-1} \hat{\mathcal{F}}_b + (\bar{M}_b \hat{M}_b^{-1} \hat{J}_b^\top - \bar{J}_b^\top) \mathcal{F}_e \end{aligned} \quad (14)$$

Proof: Taking the inertia-scaled difference in resulting locked accelerations, we obtain,

$$\begin{aligned} \hat{M}_b(\dot{\mu} - \ddot{\mu}) = & \text{ad}_{(\mu - \hat{A}_i \dot{q})}^\top \hat{M}_b \mu - \dot{\hat{M}}_b \mu + \hat{\mathcal{F}}_b + \hat{J}_b^\top \mathcal{F}_e \\ & - \hat{M}_b \bar{M}_b^{-1} (\text{ad}_{(\bar{\mu} - \bar{A}_i \dot{q})}^\top \bar{M}_b \bar{\mu} - \dot{\bar{M}}_b \bar{\mu} + \bar{\mathcal{F}}_b + \bar{J}_b^\top \mathcal{F}_e) \end{aligned} \quad (15)$$

If $\bar{\mathcal{F}}_b$ in $\bar{\mathcal{F}}_b$ is chosen as,

$$\begin{aligned} \bar{\mathcal{F}}_b = & -\bar{\mathcal{F}}_{bd} - (\text{ad}_{(\bar{\mu} - \bar{A}_i \dot{q})}^\top \bar{M}_b - \dot{\bar{M}}_b) \bar{\mu} + \bar{M}_b \hat{M}_b^{-1} \hat{\mathcal{F}}_b \\ & + \bar{M}_b \hat{M}_b^{-1} (\text{ad}_{(\mu - \hat{A}_i \dot{q})}^\top \hat{M}_b - \dot{\hat{M}}_b) \mu + (\bar{M}_b \hat{M}_b^{-1} \hat{J}_b^\top - \bar{J}_b^\top) \mathcal{F}_e \end{aligned}$$

and substituted in (15), we get, $\hat{M}_b(q)(\dot{\mu} - \ddot{\mu}) = 0_6$. In addition to this equality, if and only if, Ass. 1 holds true, we get identical $(g_b(t), \mu(t))$, and we obtain the result of the theorem by taking $\bar{\mu}(t) = \mu(t)$. ■

We note that one would obtain the same equations as (11) and (14) if the problem was formulated as an impedance control/matching task in locked and shape spaces [23, eq. 15].

B. Simulating spacecraft-base motion

In this section, we outline three proposed modalities of HLS and provide block diagrams for clarity on complete implementation using Theorems 1 and 2.

1) *Software simulation mode, M1, Fig. 4:* In this mode, the spacecraft-base motion is simulated by integrating the equations of motion. To this end, instead of using (3), we propose integrating $\mathcal{EP}(l, \xi)$ from (5), i.e. $\bar{\mathcal{F}}_b = \hat{\mathcal{F}}_b$ in Fig. 3, and (8) to close the loop as shown in Fig. 4.

2) *Impedance mode, M2, Fig. 5:* In impedance causality, the vehicle in Def. 1 has a torque-interface to effect spacecraft motion. This might be a use-case for simulating dynamics of a small-sized arm on a small satellite [24], in which the vehicle is a KUKA LWR-4, for instance. In this case, Theorem 2 is invoked to enforce a mapping, namely (14), between actuation torques $\hat{\mathcal{F}}_b, \bar{\mathcal{F}}_b$. The complete strategy has been shown in Fig. 5.

3) *Admittance mode, M3, Fig. 6:* In admittance causality, the vehicle, e.g. an industrial robot, is used in position-control mode to simulate the spacecraft motion [7]. The desired locked inertia for the admittance controller can be straightforwardly chosen as, $\hat{M}_b = \bar{M}_b$. This simplifies the map in (14) of Theorem 2 as,

$$\bar{\mathcal{F}}_b = -\bar{\mathcal{F}}_{bd} + \mathcal{EL}(l_2, \xi) - \mathcal{EL}(l, \xi) + \hat{\mathcal{F}}_b + (\hat{J}_b^\top - \bar{J}_b^\top) \mathcal{F}_e \quad (16)$$

which is substituted in (9). Satisfying Theorems 1 and 2 ensures that the OGFm motion dynamics match (5) and (7), which implies $V_b = \mu - \hat{A}_i \dot{q}$. Hence, the admittance controller commands, $(g_b(t), V_b(t))$, are obtained by integrating (9) and (8). This strategy has been shown in Fig. 6.

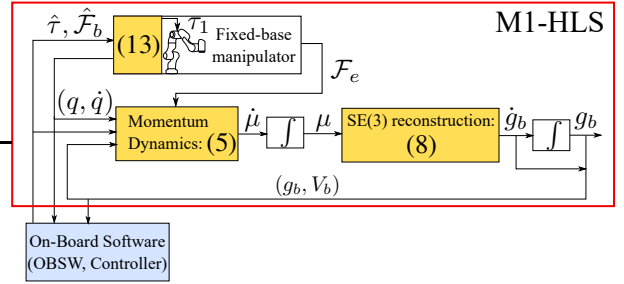


Fig. 4. A HLS setup for an orbital robot using a fixed-base OGFm.

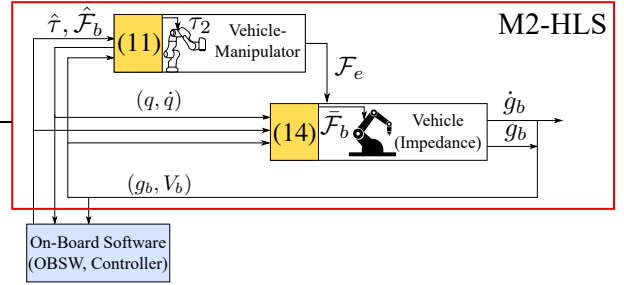


Fig. 5. A HLS setup for an orbital robot using a vehicle-manipulator with impedance causality in vehicle.

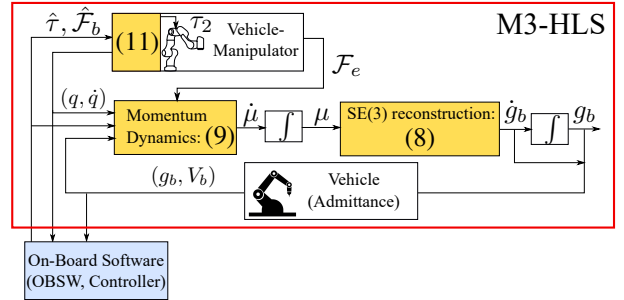


Fig. 6. A HLS setup for an orbital robot using a vehicle-manipulator with admittance causality in vehicle.

Note that the proposed methods account for different manipulator models in the OGFm and the orbital robot. A consequence of Theorems 1 and 2 is the stability M1 and M2, given that OBSW stabilizes (3). For M3, the closed-loop stability is a function of the vehicle's admittance dynamics.

VI. EXPERIMENTAL VALIDATION

In this section, the experimental results are summarized. From a practical perspective, vehicle in impedance causality (M2) has low disturbance-rejection against errors, e.g. gravity-compensation, through (14), which might affect the HLS accuracy. Therefore, results for M1 and M3 methods are shown. In both approaches, a KUKA LWR-4 was used as the manipulator for *both*, the reference orbital robot and the OGFm. The mass and inertia parameters of LWR-4 are the same as reported in [25, Table 1]. In the following, (\bullet) refers to a measured quantity. We denote the twist velocity basis of the frame $\{\mathcal{B}\}$ as e_i , $i = 1..6$ where $i = 1, 2, 3$ and $i = 4, 5, 6$ denote the instantaneous translation and rotational basis, respectively.

Scenario 1: A manipulator trajectory between two configurations was commanded while considering initial momentum $\mathcal{J}(0) = 0_6$. The OBSW was a *free-floating* controller, i.e. unactuated spacecraft. Therefore, the actuation, $(0_6, \hat{\tau})$, which was generated by the OBSW, was used in (11) to obtain τ_i commands for the two LWR-4 OGFMs. During the maneuver, contacts were made at the end-effector, $\{\mathcal{E}\}$, and the resulting wrench, \mathcal{F}_e , was measured using a F/T sensor.

For this scenario, the HLS spacecraft dynamics was computed using the following three methods.

- 1) P0: Using the complete dynamics in (3), \dot{V} was integrated with state, $(g_b, V_b, \tilde{q}, \dot{\tilde{q}})$, and actuation, $[0_6^\top \hat{\tau}^\top]^\top$, to obtain the spacecraft state, (g_b, V_b) .
- 2) P1: Using only the first row of (3), \dot{V}_b was integrated using the same actuation as P0. However, this requires $\ddot{\tilde{q}}$ measurements, which was obtained by numerical differentiation of $\dot{\tilde{q}}$ and a first order low-pass filter with cut-off frequency of 10[Hz].
- 3) M1: The proposed method was used with identical state and actuation as that of P0.

The P0 method has a dependency on $\hat{\tau}$, which results in a drift in \dot{V}_b due to the compensation of residual torques, e.g. gravity-compensation errors. Indeed, it was observed that even in static condition, the OBSW applied control action in the order of 0.1[N.m], which caused a non-physical motion in the spacecraft. Although an ad-hoc deadzone was implemented, the configuration-dependence of these torques made it ineffective. Hence, results for P1 and M1 were compared since they are independent of $\hat{\tau}$.

A. M1 on KUKA LWR-4

M1 was validated using Scenario 1 on the setup in Fig. 7, in which the reference orbital robot (Fig. 7, left) and the fixed-base OGFMs (Fig. 7, right) have been shown. A joint-space PD-controller [20] was implemented as the OBSW. The mass of the spacecraft was 105[Kg] and principal inertias were (47.5, 34.9, 46.2)[Kg.m²].

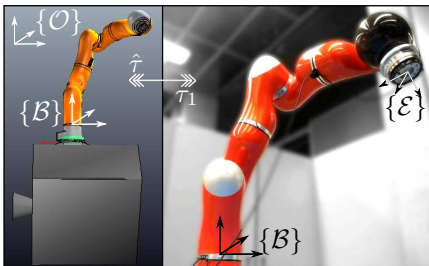


Fig. 7. M1 with KUKA LWR-4 in *both*, orbital robot and OGFMs (fixed-base). $\{\mathcal{B}\}$ is the common frame located at manipulator base of *both* systems, which are initialized with identical $(q(0), \dot{q}(0), g_b(0), \mu(0))$.

In Fig. 8, the comparison between results from P1 (left) and M1 (right) for the Scenario 1 are presented. In the first row, the measured momentum map $\tilde{\mathcal{J}}$ has been presented for both approaches in basis e_2, e_3, e_4 , since the contacts affected $\tilde{\mathcal{J}}$ in these directions by the highest magnitude. During $t = [0, 13]$ [s] (before first contact), it can be clearly seen

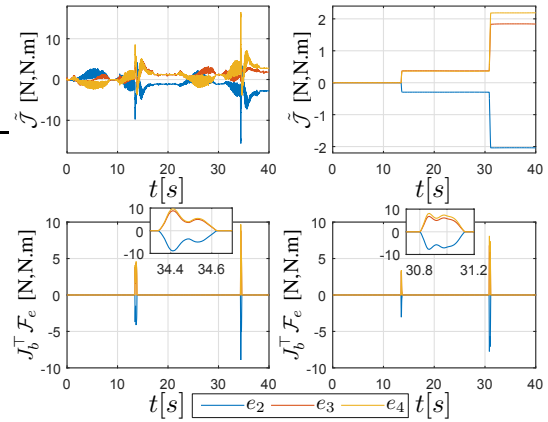


Fig. 8. Comparison between P1 (left) and M1 (right) during OGFMs motion and contacts. Top row: Momentum map, Bottom row: Contact forces. Contacts were induced manually, hence the difference in contact times.

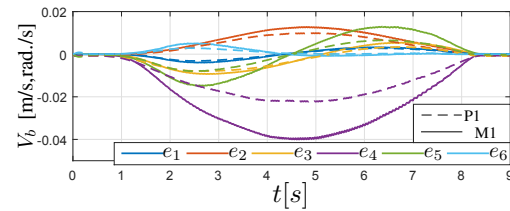


Fig. 9. Comparison of $V_b(t)$ (colored basis) during a trajectory between P1 (dashed) and M1 (solid).

that the initial condition, $\mathcal{J}(0)$, holds during manipulator motion for M1 (right), whereas in P1 (left), this condition is violated, which makes the HLS non-physical during manipulator motion. The measured contact forces referenced at $\{\mathcal{B}\}$, $J_b^\top \mathcal{F}_e$, are presented in the second row, where J_b is the spacecraft Jacobian of end-effector. Despite the applied forces being of a similar magnitude, the change in $\tilde{\mathcal{J}}(t)$ is characterized by spikes in P1 (left), whereas M1 provides consistent increments. In Fig. 9, the resulting *free-floating* spacecraft velocity V_b during $t = [0, 9]$ [s] is shown for P1 (dashed) and M1 (solid) for e_i , $i = 1..6$ (colored). Due to the non-physical momentum behavior, it can be seen that P1 results in an underestimated velocity, especially in e_4, e_5 .

B. M3 on OOS-SIM

The OOS-SIM [7] is a HLS facility (Fig. 10, right), which uses an industrial robot in *admittance* causality to simulate dynamics for the orbital robot's spacecraft. The simulated spacecraft mass was 600[Kg] and principal inertias were (500, 600, 500)[Kg.m²]. First, we note that since orbital robot and OGFMs are identical, (16) simplifies further to $\tilde{\mathcal{F}}_b = -\tilde{\mathcal{F}}_{bd} + \hat{\mathcal{F}}_b$ for the admittance controller. Secondly, (11) simplifies to $\tau_2 = -\tau_{2d} + \hat{\tau}$. Thus, the HLS simplifies to feed-through of the OBSW commands with additional gravity-compensation. For the validation procedure, \tilde{V}_b was obtained by numerically differentiating the industrial robot's forward kinematics \tilde{g}_b and using a first-order low-pass filter with 10[Hz] cut-off frequency.

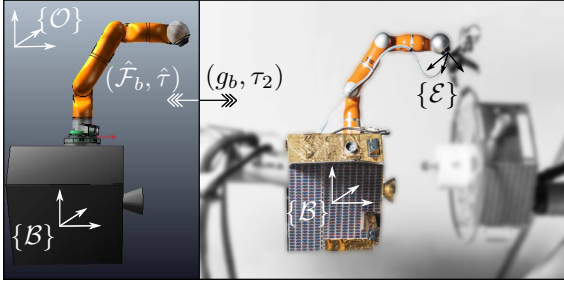


Fig. 10. M3 on OOS-SIM such that $\{B\}$ is the common frame located at spacecraft of *both* systems, which are initialized with identical $(q(0), \dot{q}(0), g_b(0), \mu(0))$.

1) *M3 in Scenario 1*: A *free-floating* Cartesian PD-controller [20] was used in Scenario 1 to approach the stationary satellite structure on the right of Fig. 10 till contact was made. The comparative results from P1 and M3 are presented in Fig. 11. In first row, $\tilde{\mathcal{J}}$ is plotted for e_1, e_3, e_5 , since the contact affected its magnitude more significantly in these basis. Note that, the second order response at $t \geq 0[s]$ in *both* approaches is due to the admittance controller's transient response. However, during $t = [0, 10]$ (plot insets), it can be seen that $\tilde{\mathcal{J}} \rightarrow 0_6$ for M3, whereas, this condition is violated for P1. This corroborates the same observation made in Sec. VI-A. We also note that, in experiments for *both*, M3 and P1, the controller parameters, trajectory and initial conditions were kept identical. However, we observe in second row that the contact duration is longer for P1. This might be explained as follows. In P1, g_b is integrated from an erroneous V_b , which was observed clearly in Fig. 9 of Sec. VI-A. This is due to a non-physical momentum, which is also seen in left of Fig. 11. As a result of the ensuing non-physical behavior, the generalized Jacobian for $\tilde{\mathcal{J}} = 0_6$, that is used in OBSW is not in agreement with HLS, resulting in modified Cartesian forces and hence a different contact behavior. In fact, a direct result of this was that the orbital robot gained *twice* as much more momentum in $t > 11[s]$ for P1 than M3.

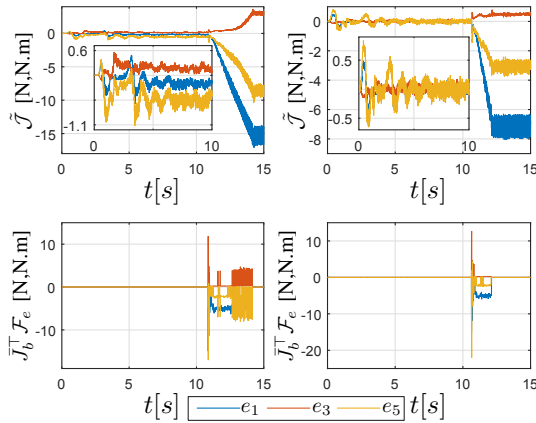


Fig. 11. Comparison between P1 (left) and M3 (right) during OGFM motion and contacts. Top row: Momentum map, Bottom row: Contact forces.

2) *M3 with spacecraft actuation*: In this scenario, the conditions of Scenario 1 were the same, however, with spacecraft actuation ($\hat{\mathcal{F}}_b \neq 0_6$). The goal of this validation was to emphasize that the proposed method is applicable to a fully-actuated orbital robot while interacting with a passive environment. A fully-actuated orbital robot controller [25] was used to regulate poses of end-effector, $\{E\}$, and spacecraft, $\{B\}$. The desired end-effector pose was chosen to induce a contact at $\{E\}$ with the client structure on right of Fig.10. The results have been presented in Fig. 12.

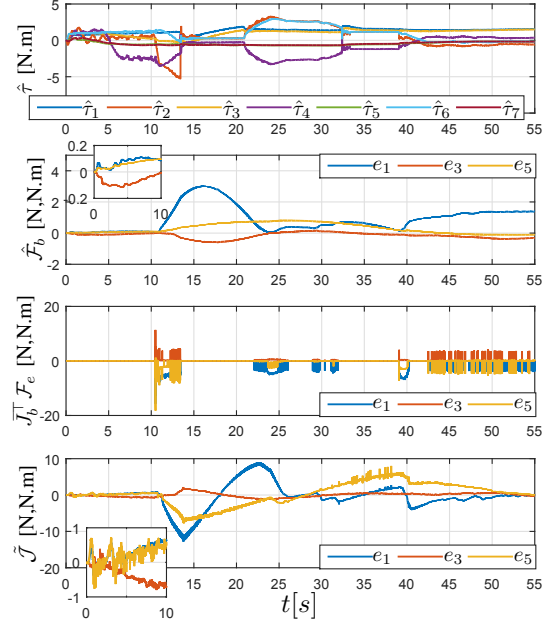


Fig. 12. Experimental result for a HLS (M3) of a fully-actuated orbital robot with multiple contacts. OBSW actuation in top two rows, contact forces in third row and momentum map in bottom row.

In the first row, the OBSW joint-actuation $\hat{\tau}$ has been plotted. The quantities $\hat{\mathcal{F}}_b$, $J_b^T \mathcal{F}_e$ and $\tilde{\mathcal{J}}$ have been plotted for e_1, e_3, e_5 bases, since the contacts affected their magnitude more significantly in these basis. Note that, as soon as the manipulator moves at $t \geq 0[s]$, $\mathcal{F}_b \neq 0_6$ (plot inset). This causes a consequent change in $\tilde{\mathcal{J}}$ (plot inset). The first contact occurs at $t = 10.5[s]$, which drastically changes $\tilde{\mathcal{J}}$. However, control action $\hat{\mathcal{F}}_b$ also increases to compensate for resulting pose errors. And finally, through consequent contacts (third row) in $t > 40[s]$, the controller is able to stabilize motion ($\tilde{\mathcal{J}} \rightarrow 0_6$, $t > 50[s]$) by achieving force balance between $\hat{\mathcal{F}}_b$ and $J_b^T \mathcal{F}_e$. This is achieved through the manipulator torques $\hat{\tau}$, which act between $\{E\}$ and $\{B\}$.

C. Discussion

In sections VI-A-VI-B, we observed that the combined effect of noisy \tilde{q} and filter dynamics in P1 negatively affects a HLS by injecting non-physical momentum during manipulator motion. This diminishes the physical consistency of HLS validation. For instance, on-ground estimation of spacecraft fuel-consumption to perform tasks, e.g. spacecraft

pose regulation, is affected by erroneous V_b and alteration of contact dynamics in P1. In contrast, the proposed M1 and M3 methods simulate an orbital robot without requiring \tilde{q} . In fact, this imparts a physically correct behaviour to the HLS without precluding external forces in dynamics. Thus, the problem statement in Sec. III-B has been duly addressed using the proposed methods and which were also experimentally validated. A key observation from Sec. VI-B is that force feedback of \mathcal{F}_e is not required to simulate interactions if the manipulators for the orbital robot and the OGFm are identical.

We remark that the proposed methods enable HLS of a fully-actuated orbital robot with contacts. However, model-based discontinuous thruster actuation requires high bandwidth in the vehicle-manipulator OGFm. In practice, time delays in the force loop and admittance characteristics might negatively affect HLS fidelity. This may limit stability during contacts, and addressing this issue with the proposed methods defines our future scope of work.

VII. CONCLUSION

In this paper, three novel hardware-in-the-loop simulation approaches were proposed to simulate a fully-actuated orbital robot in the presence of external forces. To this end, two converse theorems of Controlled Lagrangian equivalence were proved and applied to the Lagrange-Poincaré equations of an orbital robot. By exploiting the block-diagonal inertia of these equations, the need of joint acceleration/torque measurements for simulating spacecraft motion was avoided. The main benefit of the proposed approaches was physical (momentum) consistency, which was validated through experiments on *two* facilities, a fixed-base KUKA LWR-4 and OOS-SIM. Furthermore, the specific case of a fully-actuated orbital robot with multiple contacts was experimentally validated using the proposed method to prove its effectiveness.

APPENDIX

Given $g \equiv (R, p) \in \text{SE}(3)$ with body velocity twist, $\mathcal{V} = [\omega^\top \quad v^\top]^\top$, the following quantities are detailed,

$$g = \begin{bmatrix} R & p \\ 0_{1,3} & 1 \end{bmatrix}, \mathcal{V}^\wedge = \begin{bmatrix} \omega_\times & v \\ 0_{1,3} & 0 \end{bmatrix}, (\mathcal{V}^\wedge)^\vee = \mathcal{V} \quad (17)$$

$$\text{Ad}_g = \begin{bmatrix} R & p \times R \\ 0_{3,3} & R \end{bmatrix}, \text{ad}_\mathcal{V} = \begin{bmatrix} \omega_\times & v_\times \\ 0_{3,3} & \omega_\times \end{bmatrix}$$

where $(\bullet)_\times$ is a skew-symmetric matrix for the vector and, ω (v) is the angular (linear, respectively) velocity.

REFERENCES

- [1] S. Jaekel, R. Lampariello, W. Rackl, *et al.*, “Design and operational elements of the robotic subsystem for the e.Deorbit debris removal mission,” *Frontiers in Robotics and AI*, vol. 5, p. 100, 2018.
- [2] P. Colmenarejo, D. Henry, G. Visentin, *et al.*, “Methods and outcomes of the COMRADE project - Design of robust coupled control for robotic spacecraft in servicing missions,” in *International Astronautical Congress (IAC)*, Oct 2018.
- [3] H. Benninghoff, F. Rems, E. A. Risse, *et al.*, “RICADOS - rendezvous, inspection, capturing and detumbling by orbital servicing,” in *International Conference on Astrodynamics Tools and Techniques*, Nov 2018.
- [4] A. Flores-Abad, O. Ma, K. Pham, and S. Ulrich, “A review of space robotics technologies for on-orbit servicing,” *Progress in Aerospace Sciences*, vol. 68, pp. 1 – 26, 2014.

- [5] R. Lampariello, H. Mishra, N. Oumer, *et al.*, “Tracking control for the grasping of a tumbling satellite with a free-floating robot,” *IEEE Robotics and Automation Letters*, vol. 3, pp. 3638–3645, Oct 2018.
- [6] F. Aghili and J. Piedboeuf, “Hardware-in-loop simulation of robots interacting with environment via algebraic differential equation,” in *IEEE/RSJ International Conference on Intelligent Robots and Systems (IROS)*, vol. 3, pp. 1590–1596 vol.3, Oct 2000.
- [7] J. Artigas, M. De Stefano, W. Rackl, *et al.*, “The OOS-SIM: An on-ground simulation facility for on-orbit servicing robotic operations,” in *IEEE International Conference on Robotics and Automation (ICRA)*, May 2015.
- [8] H. Shimoji, M. Inoue, K. Tsuchiya, *et al.*, “Simulation system for a space robot using 6 axis servos,” *IFAC Proceedings Volumes: IFAC Symposium on Automatic Control in Aerospace*, vol. 22, pp. 115 – 120, Jul 1989.
- [9] S. K. Agrawal, G. Hirzinger, K. Landzettel, and R. Schwertassek, “A new laboratory simulator for study of motion of free-floating robots relative to space targets,” *IEEE Transactions on Robotics and Automation*, vol. 12, pp. 627–633, Aug 1996.
- [10] J. Piedboeuf, F. Aghili, M. Doyon, and E. Martin, “Dynamic emulation of space robot in one-g environment using hardware-in-the-loop simulation,” in *Romansy 14: Theory and Practice of Robots and Manipulators (CISM-IFTOMM Symposium)*, pp. 213–229, 2002.
- [11] S. Dubowsky, W. Durfee, T. Corrigan, A. Kuklinski, and U. Muller, “A laboratory test bed for space robotics: the VES II,” in *IEEE/RSJ International Conference on Intelligent Robots and Systems (IROS)*, vol. 3, pp. 1562–1569 vol.3, Sep 1994.
- [12] R. Takahashi, H. Ise, A. Konno, M. Uchiyama, and D. Sato, “Hybrid simulation of a dual-arm space robot colliding with a floating object,” *IEEE International Conference on Robotics and Automation (ICRA)*, pp. 1201–1206, 2008.
- [13] C. Carignan, N. Scott, and S. Roderick, “Hardware-in-the-loop simulation of satellite capture on a ground-based robotic testbed,” *International Symposium on Artificial Intelligence, Robotics and Automation in Space (i-SAIRAS)*, 06 2014.
- [14] A. Saccon, S. Traversaro, F. Nori, and H. Nijmeijer, “On centroidal dynamics and integrability of average angular velocity,” *IEEE Robotics and Automation Letters*, vol. 2, pp. 943–950, Apr 2017.
- [15] D. E. Chang and J. E. Marsden, “Reduction of controlled lagrangian and hamiltonian systems with symmetry,” *SIAM Journal of Control and Optimization*, vol. 43, p. 277–300, Jan 2004.
- [16] P. J. From, I. Schjølberg, J. T. Gravdahl, K. Y. Pettersen, and T. I. Fossen, “On the boundedness and skew-symmetric properties of the inertia and coriolis matrices for vehicle-manipulator systems,” *IFAC Proceedings Volumes: IFAC Symposium on Intelligent Autonomous Vehicles*, vol. 43, no. 16, pp. 193 – 198, 2010.
- [17] A. M. Bloch, P. S. Krishnaprasad, J. E. Marsden, and R. M. Murray, “Nonholonomic mechanical systems with symmetry,” *Archive for Rational Mechanics and Analysis*, vol. 136, pp. 21–99, Dec 1996.
- [18] A. Beyer, G. Grunwald, M. Heumos, M. Schedl, R. Bayer, *et al.*, “CAESAR: Space robotics technology for assembly, maintenance, and repair,” in *International Astronautical Congress (IAC)*, 2018.
- [19] D. E. Chang, *Controlled Lagrangian and Hamiltonian systems*. PhD thesis, California Institute of Technology, 2002.
- [20] K. Yoshida and D. N. Nenchev, “A general formulation of under-actuated manipulator systems,” in *Robotics Research*, pp. 33–44, Springer London, 1998.
- [21] G. Garofalo, B. Henze, J. Engelsberger, and C. Ott, “On the inertially decoupled structure of the floating base robot dynamics,” *IFAC-PapersOnLine: International Conference on Mathematical Modelling*, vol. 48, no. 1, pp. 322 – 327, 2015.
- [22] R. M. Murray, “Nonlinear control of mechanical systems: A Lagrangian perspective,” *Annual Reviews in Control*, vol. 21, pp. 31 – 42, 1997.
- [23] N. Hogan, “Impedance Control: An Approach to Manipulation: Part II—Implementation,” *Journal of Dynamic Systems, Measurement, and Control*, vol. 107, pp. 8–16, 03 1985.
- [24] M. Maier, M. Chalon, M. Pfanne, R. Bayer, *et al.*, “TINA: small torque controlled robotic arm for exploration and small satellites,” in *International Astronautical Congress (IAC)*, 2019.
- [25] M. De Stefano, R. Balachandran, A. M. Giordano, C. Ott, and C. Secchi, “An energy-based approach for the multi-rate control of a manipulator on an actuated base,” in *IEEE International Conference on Robotics and Automation (ICRA)*, pp. 1072–1077, May 2018.